

# CHAPTER 3

## Collapse prediction and creep effects

P.B. Lourenço & J. Pina-Henriques

*Department of Civil Engineering, University of Minho, Portugal.*

### 3.1 Introduction

The collapse of the Pavia Civic Tower in 1989 was an event of great concern for the public authorities and for the technical community. The collapse rapidly became a focus of interest among masonry researchers and several masonry blocks were recovered from the ruins for mechanical and physical/chemical laboratory testing [1]. Such tests permitted to identify the time-dependent mechanical damage of the tower walls due to high sustained loading as the possible main cause of collapse.

The tower of Pavia is not an isolated case and several other famous examples can be mentioned, such as the collapse of the St. Magdalena bell-tower in Goch, Germany, in 1993, the partial collapse of the Noto Cathedral, Italy, in 1996, and the severe damage exhibited by the bell-tower of the Monza Cathedral, Italy.

Masonry creep depends mainly on factors such as the stress level and the temperature/humidity conditions but cyclic actions, such as wind, temperature variations or vibrations induced by traffic or ringing bells, in the case of bell towers, have a synergetic effect, increasing material damage. For these reasons, high towers and heavily stressed columns are the structural elements where severe time-dependent damage can occur [2].

Traditionally, three creep stages can be recognized: a *primary* stage where the creep rate decreases gradually, a *secondary* stage where the creep rate remains approximately constant and a *tertiary* stage where the creep rate increases rapidly towards failure. A sufficiently high stress level must be applied so that the last two stages are initiated. In the secondary stage, diffuse and thin vertical cracking propagates and coalesces into macro-cracks that may lead, possibly, to creep failure of the material. Creep of cementitious materials is generally attributed to crack growth and interparticle bond breakage due to moisture seepage. In fact, under



sustained loading, forced moisture redistribution can occur in the pore structure of the material causing debonding and rebonding of the micro-structure particles [3]. In the case of concrete or new masonry, if drying shrinkage is occurring simultaneously to creep, the time-dependent deformation is increased due to a coupled effect known as the *Pickett effect* [4]. Time-dependent deformation in a constant hygral and thermal environment, and in the absence of cracking, is denominated by *basic creep* (see, e.g., Neville [5], and the reader is referred to Van Zijl [6] for a comprehensive discussion on the viscous behaviour of masonry).

For low stress levels, below 40 to 50% of the compressive strength, only primary creep is present and creep deformation can be assumed proportional to the stress level. References on masonry creep within the elastic range are rather abundant in literature, [7–9]. On the contrary, creep under high stresses, even in the case of concrete, is not a sufficiently debated issue [10–12]. The fact that standard design methods for new structures are based on linear elastic material hypothesis has contributed to the diminished interest of researchers on this topic. However, ancient masonry structures are often functioning under low safety margins according to modern safety regulations. This can be due to inadequate knowledge of mechanics or due to the structural modifications that occurred along centuries, resulting in overweighting of the structure and rendering importance to non-linear creep.

Detailed modelling approaches in which units and mortar are individually represented are of great interest in understanding the phenomena occurring at the constituent level. In particular, insight into stress redistribution and damage growth occurring under sustained loading can be provided. However, before introducing long-term effects, knowledge of the short-term behaviour and governing failure mechanisms is of fundamental importance. Nevertheless, numerical prediction of the short-term response of masonry based on the properties of the constituents remains unresolved [13]. In Section 3.2, an attempt to provide reliable predictions of the compressive strength of masonry and a discussion of the observed failure mechanisms are discussed. A standard continuum model, based on plasticity and cracking, and a particle model developed in discrete settings have been considered to represent units and mortar. In Section 3.3, an experimental investigation into the behaviour of ancient masonry under high compressive stresses is described and its results are carefully analysed. Standard uniaxial compression tests, short-term creep tests and long-term creep tests were considered with the aim of presenting a comparative discussion.

## 3.2 Short-term compression: failure analysis and collapse prediction using numerical simulations

### 3.2.1 Experimental results

Binda *et al.* [14] carried out deformation controlled tests on masonry prisms with dimensions of  $600 \times 500 \times 250 \text{ mm}^3$ , built up with nine courses of



Table 3.1: Mechanical properties of the masonry components [14].

Component	$E$ (N/mm <sup>2</sup> )	$\nu$	$f_c$ (N/mm <sup>2</sup> )	$f_f$ (N/mm <sup>2</sup> )
Unit	4865	0.09	26.9	4.9
Mortar M1	1180	0.06	3.2	0.9
Mortar M2	5650	0.09	12.7	3.9
Mortar M3	17760	0.12	95.0	15.7

Table 3.2: Mechanical properties of the masonry prisms [14].

Prism type	Mortar type	$E$ (N/mm <sup>2</sup> )	$f_c$ (N/mm <sup>2</sup> )
P1	M1	1110	11.0
P2	M2	2210	14.5
P3	M3	2920	17.8

250 × 120 × 55 mm<sup>3</sup> solid soft mud bricks and 10 mm thick mortar joints. Three different types of mortar, denoted as M1, M2 and M3, have been considered and testing aimed at the evaluation of the compressive properties of the prisms. For each type of mortar, a total of three prisms were tested.

The tests were carried out in a uniaxial testing machine MTS<sup>®</sup> 311.01.00, with non-rotating steel plates and a maximum capacity of 2500 kN. The applied load was measured by a load cell located between the upper plate and the testing machine, while the average vertical displacement was recorded with the machine's in-built displacement transducer, permitting one to capture the complete stress-strain diagram, including the softening regime.

The characteristics of the masonry components in terms of compressive strength  $f_c$ , flexural tensile strength  $f_f$ , elastic modulus  $E$  and coefficient of Poisson  $\nu$  are given in Table 3.1. The results obtained for the prisms are given in Table 3.2. Prisms P1, P2 and P3 were built with mortars M1, M2 and M3 of increasing strength, respectively. The experimental failure patterns found were rather similar despite the type of mortar used [15]. Figure 3.1 depicts the typical failure pattern.

### 3.2.2 Continuum model

The simulations were carried out resorting to a *basic cell*, i.e. a periodic pattern associated to a frame of reference (see Fig. 3.2), in which units and mortar were represented by a structured continuum finite element mesh. However, in order to reduce computational effort only a quarter of the basic cell was modelled assuming symmetry conditions for the in-plane boundaries (see Fig. 3.3). The dimensions of the components are equal to the ones used in the experiments. It is emphasized that the adopted approach is only an approximation of the real geometry

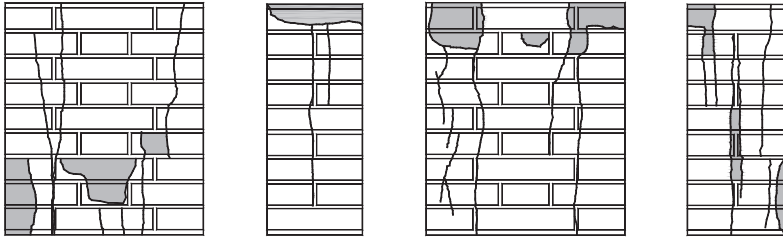


Figure 3.1: Typical experimental failure patterns [15]. The shaded areas indicate spalling of material.

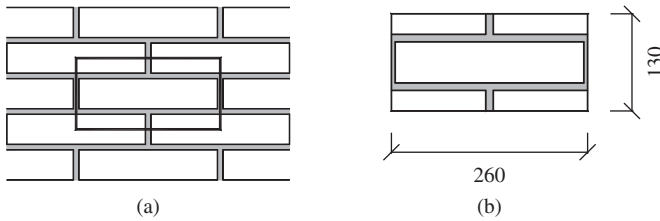


Figure 3.2: Definition of basic cell: (a) running bond masonry and (b) geometry.

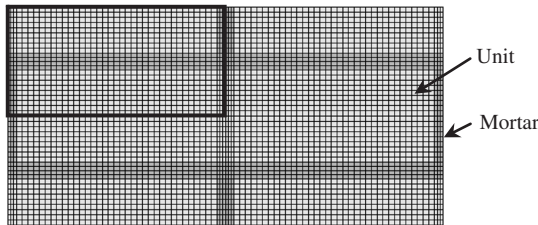


Figure 3.3: Continuum model used in the simulations (only the indicated quarter was simulated, assuming symmetry conditions).

and that the obtained numerical response is phenomenological, which means that a comparison in terms of experimental and numerical failure patterns is not possible. In particular, splitting cracks usually observed in prisms tested under compression [16], boundary effects of the specimen and non-symmetric failure modes are not captured by the numerical analysis. Nevertheless, most of these effects control mainly the post-peak response, which is not the key issue in the present contribution.

Three different plane approaches have been considered taking into account the out-of-plane boundaries, namely: (a) plane-stress (PS), (b) plane-strain (PE) and (c) an intermediate state, here named enhanced-plane-strain (EPE). This last approach consists in modelling a thin out-of-plane masonry layer with 3D elements, imposing

equal displacements in the two faces of the layer. Full 3D analyses with refined meshes and softening behaviour are unwieldy, and were not considered. Moreover, recent research indicated that enhanced-plane-stress analysis provides very similar results [17]. EPE response is always between the extreme responses obtained with PS and PE. For this reason, EPE is accepted as the reference solution for the continuum simulations and only its results are considered in this paper. A complete description of the continuum simulations can be found in Pina-Henriques and Lourenço [18].

Modelling of the cell in EPE was carried out using approximately 900 20-noded brick elements with 6650 nodes, totalling 13,300 degrees of freedom (note that the tying adopted for the out-of-plane degrees of freedom mean that, basically, a 2D model is used). The integration used was  $3 \times 3 \times 3$  Gauss. The material behaviour was described using a composite model including a traditional smeared crack model in tension, specified as a combination of tension cut-off (two orthogonal cracks), tension softening and shear retention [19], and a Drucker-Prager plasticity model in compression [20]. The inelastic behaviour exhibits a parabolic hardening/softening diagram in compression and an exponential-type softening diagram in tension. The material behaves elastically up to one-third of the compressive strength and up to the tensile strength.

In order to reproduce correctly the elastic stiffness of the masonry prisms, the experimental elastic modulus of the mortar  $E$  must be adjusted by inverse fitting. In fact, the mortar experimental stiffness leads to a clear over stiff response of the numerical specimens. This can be explained by the fact that the mechanical properties of mortar inside the composite are different from mortar specimens cast separately. This is due to mortar laying and curing and represents a severe drawback of detailed micro-models. The material properties adopted, including the adjusted mortar stiffness values  $E^*$  are fully detailed in Table 3.3. Here,  $c$  is the cohesion,  $f_t$  is the tensile strength,  $\phi$  is the friction angle,  $\psi$  is the dilatancy angle,  $G_{ft}$  is the tensile fracture energy and  $G_{fc}$  is the compressive fracture energy. The value adopted for the friction angle was  $10^\circ$  (a larger value in plane-stress would implicate an overestimation of the biaxial strength) and, for the dilatancy angle, a value of  $5^\circ$  was assumed [21]. The values assumed for the fracture energy have been based on recommendations supported by experimental evidence [22, 23], and practical requirements to ensure numerical convergence.

Table 3.3: Inelastic properties given to masonry components.

Component	$E^*$ (N/mm <sup>2</sup> )	$c$ (N/mm <sup>2</sup> )	$f_t$ (N/mm <sup>2</sup> )	$\sin \phi$	$\sin \psi$	$G_{ft}$ (N/mm)	$G_{fc}$ (N/mm)
Unit	4865	11.3	3.7	0.17	0.09	0.190	12.5
Mortar M1	355	1.3	0.7	0.17	0.09	0.350	2.7
Mortar M2	735	5.3	3.0	0.17	0.09	0.150	10.0
Mortar M3	1065	39.9	12.0	0.17	0.09	0.600	23.0

\*In the case of mortars, the values refer to the adjusted stiffness values.



### 3.2.3 Particle model

The 2D particle model supposed to represent the micro-structure of units and mortar consists of a phenomenological discontinuum approach based on the finite element method including interface elements. The discontinuous nature of the masonry components is considered by attributing a fictitious micro-structure to units and mortar, which is composed by linear elastic continuum elements of polygonal shape (hereafter named particles) separated by non-linear interface elements. All inelastic phenomena occur in the interfaces and the process of fracturing consists of progressive bond-breakage. This is, of course, a phenomenological approach, able, nevertheless, to capture the typical failure mechanisms and global behaviour of quasi-brittle materials. For a detailed discussion of the model, including proposals for selection of numerical data, sensitivity studies, fracture processes and failure mechanisms, and size effect studies, the reader is referred to Pina-Henriques and Lourenço [13]. There, it is also shown that the compressive and tensile strength values yielded by the model can be considered as independent from particle size and particle distortion for practical purposes.

The constitutive model used for the interface elements was formulated by Lourenço and Rots [24] and is implemented in the finite element code adopted for the analyses [20]. The model includes a tension cut-off for tensile failure (mode I), a Coulomb friction envelope for shear failure (mode II) and a cap mode for compressive failure. Exponential softening is present in all three modes and is preceded by hardening in the case of the cap mode. Micro-structural disorder is considered in the model by the irregular geometry of the particles and by attributing to particles and interfaces randomly generated material properties, according to a Gaussian distribution, for given values of the average and coefficient of variation of the material parameters.

The particle model simulations were carried out employing the same basic cell used for the continuum model (see Fig. 3.2). The particle model is composed by approximately 13,000 linear triangular continuum elements, 6000 linear line interface elements and 15,000 nodes (see Fig. 3.4). Macro homogeneous symmetry conditions have been assumed.

The material parameters were defined by comparing the experimental and numerical responses of units and mortar considered separately. Each material was modelled

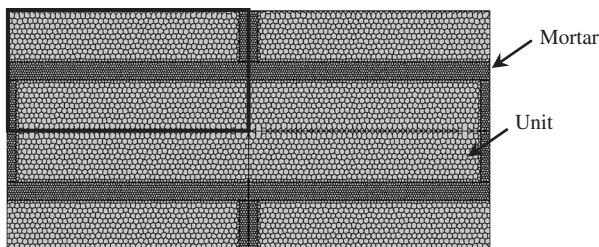


Figure 3.4: Particle model of the masonry cell (only the quarter indicated was simulated, assuming symmetry conditions).

resorting to specimens with the same average particle size, mesh distortion and dimensions of the masonry components used in the composite model (basic cell).

Given the stochastic nature of the model, five simulations were performed for each masonry component assuming equal average values for the model material parameters. The parameters were obtained, whenever possible, from the experimental tests described in Section 3.2.1, but most of the inelastic parameters were unknown and had to be estimated. For the particles, average elastic modulus  $E$  values larger than the experimental ones had to be adopted due to the contribution of the interfaces deformability, characterized by  $k_n$  and  $k_s$ , to the overall deformability of the specimen. This correction is necessary despite the high dummy stiffnesses assumed.

On the contrary, the values adopted for the interfaces tensile strength  $f_t$  are slightly lower than the experimental tensile strength of the specimens, given the contribution of the interfaces shear strength due to the irregular fracture plane. The cohesion  $c$  was taken, in general, equal to  $1.5 f_t$  [25]. However, quite low experimental ratios between the compressive and tensile strengths were reported for the units and mortars considered here, with values ranging between four and eight. Due to this reason, cohesion values lower than  $1.5 f_t$  had to be adopted for mortars M1 and M2.

The values for the friction coefficient  $\tan\phi$  were adopted so that the numerical compressive strength showed a good agreement with the experimental strength. The values assumed for mode I fracture energy  $G_{fI}$  have been based on recommendations supported in experimental evidence [23, 26]. For mode II fracture energy  $G_{fII}$ , a value equal to  $0.5c$  was assumed, with the exception of the very high strength mortar M3, for which a lower value equal to  $0.3c$  was adopted. The complete material parameters adopted are given in Table 3.4 and, for such input, the response obtained is given in Table 3.5.

### 3.2.4 Discussion of the results

The numerical results obtained for the masonry prisms considering the mortar experimental  $Num\_E$  and adjusted  $Num\_E^*$  stiffnesses are given in Table 3.6,

Table 3.4: Values assumed for the material parameters (in brackets, the coefficient of variation is given in %).

		Unit	M1	M2	M3
Particles	$E^*$ (N/mm <sup>2</sup> )	6000 (30)	355 (30)	750 (30)	1200 (30)
	$\nu$	0.09 (0)	0.06 (0)	0.09 (0)	0.12 (0)
Interfaces	$k_n$ (N/mm <sup>3</sup> )	$1 \times 10^4$ (0)			
	$k_s$ (N/mm <sup>3</sup> )	$1 \times 10^4$ (0)			
	$f_t$ (N/mm <sup>2</sup> )	3.40 (45)	0.75 (45)	3.50 (45)	10.50 (45)
	$G_{fI}$ (N/mm)	0.170 (45)	0.038 (45)	0.175 (45)	0.525 (45)
	$c$ (N/mm <sup>2</sup> )	5.10 (45)	0.30 (45)	0.70 (45)	15.75 (45)
	$G_{fII}$ (N/mm)	2.55 (45)	0.15 (45)	0.35 (45)	3.15 (45)
	$\tan\phi$	0.10 (45)	0.00 (0)	0.00 (0)	0.10 (45)

\*In the case of mortars, the values refer to the adjusted stiffness values.



Table 3.5: Numerical response obtained for the masonry components (in brackets, the coefficient of variation is given in %).

	Unit	M1	M2	M3
$f_c$ (N/mm <sup>2</sup> )	27.2 (2.7)	3.2 (5.0)	12.7 (5.4)	95.8 (4.4)
$f_t$ (N/mm <sup>2</sup> )	3.61 (1.4)	0.64 (4.7)	2.70 (4.2)	11.62 (6.6)
$E$ (N/mm <sup>2</sup> )	4786 (1.9)	1309 (1.4)	5632 (3.0)	17176 (3.1)

Table 3.6: Experimental results (*Exp*) and numerical results using experimental *Num\_E* and adjusted *Num\_E\** mortar stiffness values.

Prism type		Continuum model			Particle model		
		P1	P2	P3	P1	P2	P3
$f_c$ (N/mm <sup>2</sup> )	<i>Exp</i>	11.0	14.5	17.8	11.0	14.5	17.8
	<i>Num_E</i>	19.8	24.2	31.0	15.5	19.3	30.8
	<i>Num_E*</i>	18.2	24.1	30.0	15.4	17.3	24.6
$\varepsilon_p$ (10 <sup>-3</sup> )	<i>Exp</i>	10.5	7.9	6.6	10.5	7.9	6.6
	<i>Num_E</i>	10.6	9.7	8.4	5.4	4.6	6.2
	<i>Num_E*</i>	19.9	16.0	33.5	11.8	8.1	8.9

where  $f_c$  is the compressive strength and  $\varepsilon_p$  is the peak strain. In addition, the prisms experimental results are shown for a better comparison. It is noted, however, that the reference solution for the numerical simulations is the solution provided by *Num\_E\**. Figure 3.5 depicts the experimental and numerical stress–strain diagrams.

From the given results, it is clear that the experimental collapse load is overestimated by the particle and continuum models, and that the predicted strength is affected by the mortar stiffness, especially in the case of the particle model. However, a much better agreement with the experimental strength and peak strain has been achieved with the particle model, when compared to the continuum model. In fact, the numerical over experimental strength ratios ranged between 165 and 170% in the case of the continuum model while in the case of the particle model, strength ratios ranging between 120 and 140% were found. The results obtained also show that the peak strain values are well reproduced by the particle model but large overestimations are obtained with the continuum model. For this last model, experimental over numerical peak strain ratios ranging between 190 and 510% were found.

Failure patterns are an important aspect when assessing numerical models. The (incremental) deformed meshes near failure using the continuum and particle models are depicted in Fig. 3.6–3.8 for prisms P1 to P3, respectively. In case of the continuum model, the contour of the minimum principal plastic strains is also given for a better interpretation of the mechanisms governing failure. It is noted that despite the fact that only a quarter of the basic cell has been modelled the results are shown in the entire basic cell to obtain more legible figures.

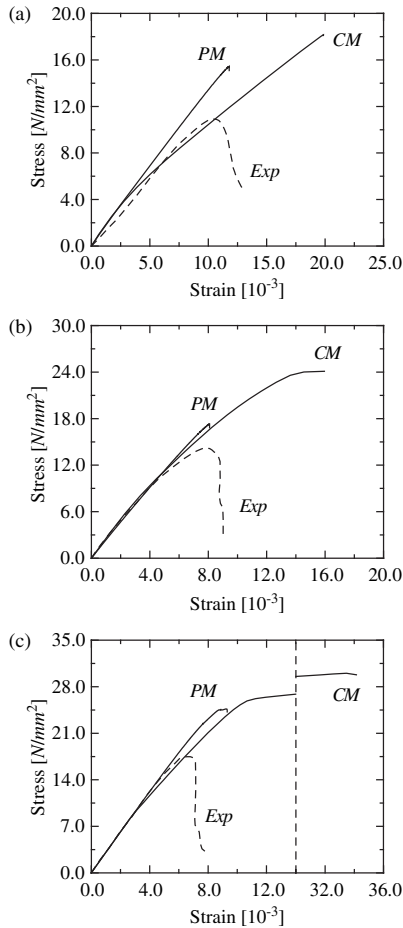


Figure 3.5: Numerical and experimental stress–strain diagrams, using adjusted mortar stiffness values, for prisms: (a) P1, (b) P2 and (c) P3. In the diagrams *CM* stands for continuum model, *PM* for particle model and *Exp* for experimental data.

The numerical failure patterns obtained are similar for both continuum and particle models. Even if the proposed particle model approach is phenomenological, the failure patterns resemble well typical compression experimental patterns observed in the face of masonry specimens. In the case of prism P1, failure occurs mainly due to the development of vertical cracks in the centre of the units and along the head-joints, being the mortar in the bed-joints severely damaged. Prism P2 fails due to diffuse damage developing in units and mortar in a rather uniform manner. In the case of prism P3, diffuse damage is also present but localized crushing of the units can be clearly observed at one-half and one-sixth of the length of the masonry units.

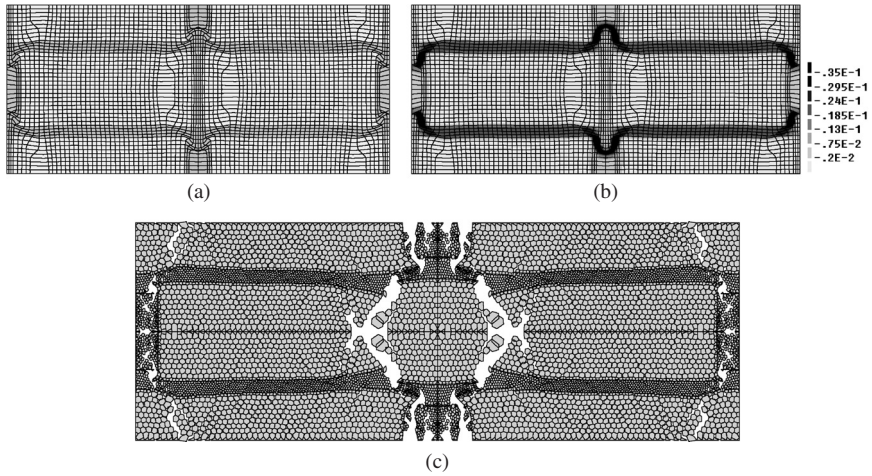


Figure 3.6: Results at failure for prism P1 using the continuum model: (a) deformed (incremental) mesh and (b) minimum principal plastic strains; and using the particle model: (c) deformed incremental mesh.

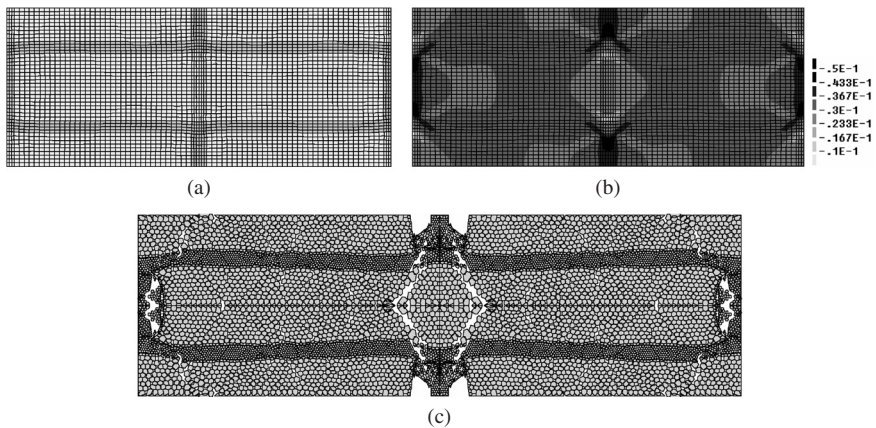


Figure 3.7: Results at failure for prism P2 using the continuum model: (a) deformed (incremental) mesh and (b) minimum principal plastic strains; and using the particle model: (c) deformed incremental mesh.

### 3.3 Long-term compression: experimental assessment

#### 3.3.1 Tested specimens

The experimental investigation was carried out on ancient masonry prisms due to the difficulty of producing laboratory specimens that correctly represent the

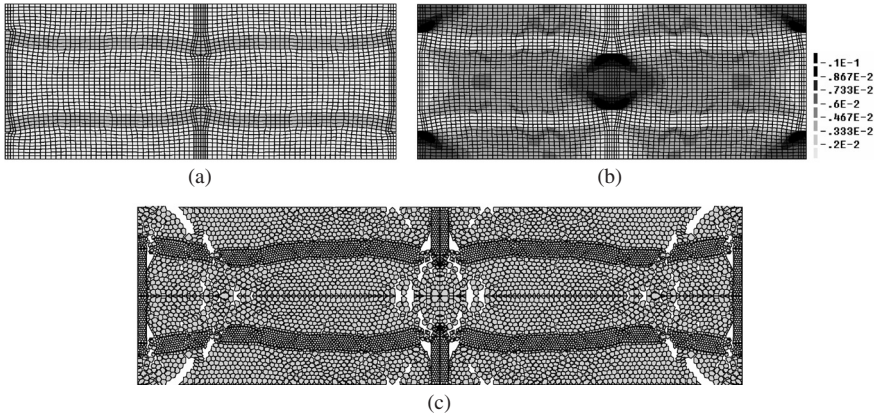


Figure 3.8: Results at failure for prism P3 using the continuum model: (a) deformed (incremental) mesh and (b) minimum principal plastic strains; and using the particle model: (c) deformed incremental mesh.

Table 3.7: Number of specimens  $n$  for each type of test.

	$n$
Compression	4
Short-term creep	4
Long-term creep	6

material typically found in historical masonry structures. Major obstacles to fabricate specimens are mortar carbonation, hardening or setting, which have a significant influence on the viscous behaviour of masonry and cannot be adequately reproduced in new specimens. On the other hand, the high cost and very limited number of ancient masonry specimens available for destructive testing are obvious. As previous experience with similar materials in the scientific community is not frequent [2], the current testing program was much relevant as it represents a learning process. In particular, recommendations for testing such specimens could only be given at the end of the testing program.

The experimental investigation carried out focuses on regular coursed brick masonry specimens PRe recovered from the ruins of the belfry of the Pavia Civic Tower. The dimensions of the specimens were  $(200 \pm 5) \times (200 \pm 5) \times (330 \pm 20)$  mm<sup>3</sup>. Before subsequent testing under compression, the loaded faces of the prisms were regularized with a cement based mortar layer approximately 10 mm thick. In all tests, Teflon sheets were introduced between the prisms and the loading plates to minimize restraining frictional stresses. A summary of the tests performed is given in Table 3.7.

### 3.3.2 Standard compression tests

Standard compression tests were conducted on four specimens. The tests were partly carried out in University of Minho (specimens PRe\_1 and PRe\_2) and in Politecnico di Milano (specimens PRe\_3 and PRe\_4). The specimens had to be tested with different test setups according to the conditions locally available at each laboratory. In this way, the tests performed in University of Minho were carried out in a uniaxial hydraulic testing machine with non-rotating steel plates and a maximum capacity of 2000 kN. The load was monotonically increased under displacement control at the rate of 4  $\mu\text{m/s}$ . The applied load was measured by a load cell located between the upper plate and the testing machine, and displacements in the specimens were recorded by two vertical inductive displacement transducers HBM (10 mm range), positioned at two different faces of the prisms and by two horizontal transducers positioned at the other two faces.

The tests performed in Politecnico di Milano were carried out using a uniaxial servo-controlled MTS<sup>®</sup> 311.01.00 testing machine, with non-rotating steel plates and a maximum capacity of 2500 kN. Loading was applied under displacement control at a rate of 1  $\mu\text{m/s}$ . The applied load was recorded by a load cell and displacements were measured with one vertical and one horizontal displacement transducers GEFRAN PY2-10 (10 mm range) positioned at each face of the prisms. For all tested specimens, longitudinal displacements were measured over approximately 200 mm span and transversal displacements over about 150 mm span.

The results obtained are illustrated in Fig. 3.9. Here, the negative sign is adopted for contraction (longitudinal or vertical strains  $\epsilon_v$ ) and the positive sign is adopted for elongation (transversal or horizontal strains  $\epsilon_h$ ). It is noted that the null horizontal deformations exhibited up to the peak load in the case of specimen PRe\_1 can be explained by the fact that only two horizontal transducers per specimen were used. Table 3.8 gives a summary of the test results in terms of the elastic modulus  $E$ , compressive strength  $f_c$  and peak strain  $\epsilon_p$ . The elastic modulus was

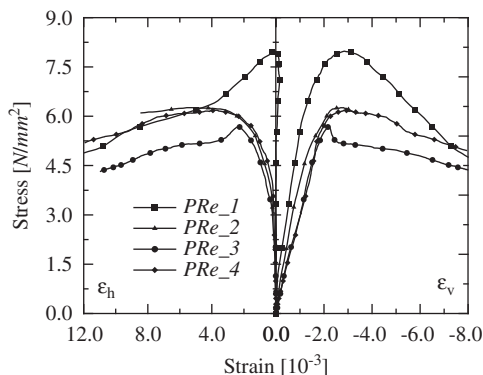


Figure 3.9: Stress–strain diagrams obtained from standard compression tests.

Table 3.8: Results obtained from standard compression tests (in brackets, the coefficient of variation is given).

Specimen	$E$ (N/mm <sup>2</sup> )	$f_c$ (N/mm <sup>2</sup> )	$\varepsilon_p$ (10 <sup>-3</sup> )
Pre_1	4980	8.0	2.7
Pre_2	4515	6.3	2.9
Pre_3	2510	5.7	2.2
Pre_4	2720	6.2	3.0
Average	3680 (34%)	6.6 (15%)	2.7 (13%)

calculated as the average slope of the stress–strain diagram between 30 and 50% of  $f_c$ . It is noted that the elastic modulus is the parameter showing the largest coefficient of variation, approximately the double of the values found for the strength and peak strain.

### 3.3.3 Short-term creep tests

#### *Experimental set-up*

Short-term creep tests were carried out at Politecnico di Milano using, again, the uniaxial servo-controlled MTS<sup>®</sup> 311.01.00 testing machine. The experimental tests considered in this section are part of an extensive testing program under development at the Politecnico di Milano, which is thoroughly described in Chapter 2. The displacements in the specimens were recorded by a vertical and a horizontal displacement transducer GEFTRAN PY2-10 (10 mm range) positioned in each face of the prisms, in a total of eight transducers per specimen. Vertical transducers measured the average longitudinal deformation over approximately 200 mm span and horizontal transducers measured the average transversal deformation over approximately 150 mm span.

#### *Testing program*

A total of four specimens were tested for short-term creep. In standard creep tests, a specimen is subjected to a constant load and strain is recorded at subsequent times. Reproduction of the test with a series of different loads gives a family of creep curves, which characterize the creep behaviour of the material. However, in the case of ancient masonry, this procedure has severe drawbacks due to the high scatter of the material strength and the limited number of specimens available. To overcome these problems and to obtain as much information as possible from each specimen, a stepped load-time diagram has been applied to the specimens.

The specimens were tested by applying successive load steps of 0.30 N/mm<sup>2</sup> at intervals of eight hours. In this way, failure could occur either during the loading phase (short-term failure) or during sustained loading (tertiary creep). An attempt to obtain creep failure of the specimens was pursued by increasing the duration of the last steps whenever the strain rate was similar to the values observed in previously tested specimens. This issue will be further addressed in Section 3.3.5.



### Test results

Figure 3.10a depicts the average vertical (longitudinal) and horizontal (transversal) strains obtained, respectively  $\varepsilon_v$  and  $\varepsilon_h$ . Figure 3.10b illustrates, as an example, the time–stress–strain diagram for specimen PRe\_5, which provides a detailed description of the results. In addition, Table 3.9 gives a summary of the experimental results in terms of the elastic modulus  $E$ , peak stress  $f'_c$  and time to failure  $T$ , which corresponds to the duration of the creep test. The values for the elastic modulus  $E$  were calculated as an average from the second to fourth load steps (0.30–1.2 N/mm<sup>2</sup>).

The sample is too small to extract any conclusion. Nevertheless, the comparison between the average standard compression strength ( $f_c = 6.6$  N/mm<sup>2</sup>) and the

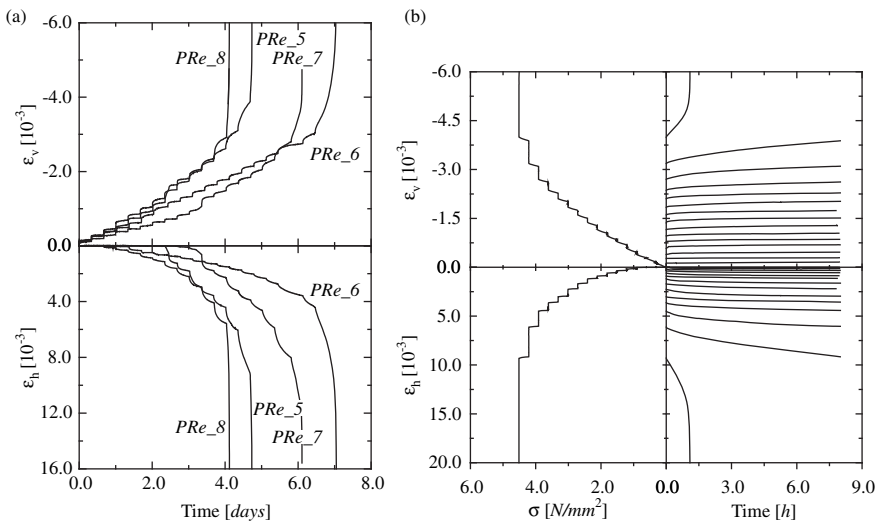


Figure 3.10: Results obtained from short-term creep tests: (a) strain–time diagrams for all tested specimens and (b) time–stress–strain diagram for specimen PRe\_5.

Table 3.9: Results obtained from short-term creep tests (in brackets, the coefficient of variation is given).

Specimen	$E$ (N/mm <sup>2</sup> )	$f'_c$ (N/mm <sup>2</sup> )	$T$ (days)
PRe_5	2700	4.50	4.7
PRe_6	3185	5.70	7.0
PRe_7	4075	5.40	6.1
PRe_8	3815	3.90	4.1
Average	3445 (18%)	4.9 (17%)	5.4



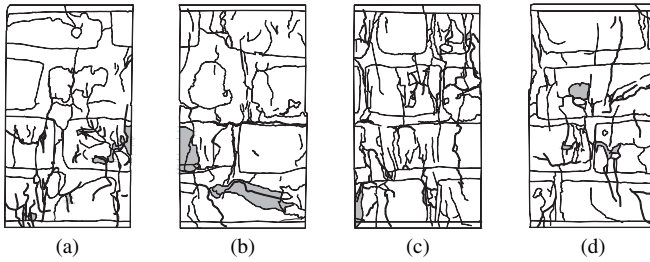


Figure 3.11: Failure pattern for specimen PRe\_7. Shaded areas indicate spalling/loss of material.

average short-term creep strength ( $f_c' = 4.9 \text{ N/mm}^2$ ) seems to indicate that damage growth due to sustained loading influenced the results. In terms of average elastic modulus, the difference is rather small.

With respect to crack patterns, thin and diffuse vertical cracks developed in the specimens during testing but large cracks and spalling were observed only at failure. This failure mode is particularly dangerous as it can lead to erroneous conclusions about the safety level of existing structures. Figure 3.11 illustrates, as an example, the failure pattern for specimen PRe\_7.

### 3.3.4 Long-term creep tests

#### *Experimental set-up*

Long-term creep tests require specific testing equipment able to keep the load constant for long periods. In this study, three steel frames were specially designed and built to perform the tests conducted at University of Minho, see Fig. 3.12a and b. Each frame includes two loading steel plates, a hydraulic jack, a pressure gauge and a gas reservoir to stabilize the applied load. The lower steel plate was fixed, while the upper plate was hinged. The equipment was designed to test two prisms simultaneously, separated by a steel plate. Upon failure of one of the specimens, the equipment is unloaded to remove the failed specimen and re-loaded with the remaining specimen. Further references on long-term creep tests can be found in [27].

Longitudinal and transversal deformations were measured on each face of the prisms with a removable strain-gauge Laser electronic TP (see Fig. 3.12c). Longitudinal deformations were measured over three mortar bed-joints with an approximate span of 250 mm, while transversal deformations were measured over one head-joint with an approximate span of 145 mm. In addition, one inductive transducer HBM (10 mm range) per specimen was employed in the longitudinal direction to act as control of the strain-gauge measurements. It is noted that in the face of the specimen where the transducer was placed, the transversal displacement was not measured. In this way, the average longitudinal displacement of each specimen results from four strain-gauge measurements, while the transversal

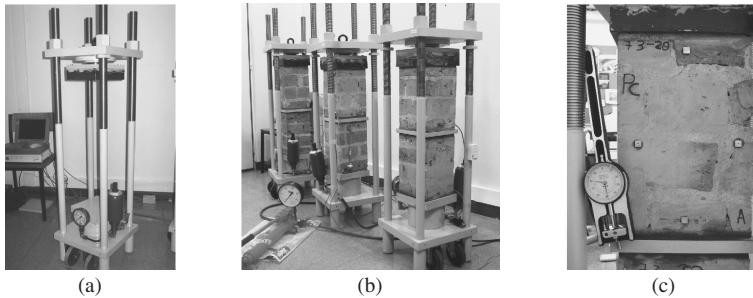


Figure 3.12: Testing apparatus: (a) hydraulic frame, (b) specimens under testing and (c) removable strain gauge and contact seats glued to the specimen.

displacement results from three strain-gauge measurements. The tests were carried out under controlled conditions of temperature ( $22 \pm 2^\circ\text{C}$ ) and humidity ( $55 \pm 10\%$ ), which were recorded by a data logger Testostor 175-2.

#### *Testing program*

The tests were conducted on six specimens. As in short-term creep tests, the load was applied by successive steps and kept constant for a given period. Two different load histories have been considered in order to better define future testing programs in similar specimens. A total of two prisms were tested by applying an initial stress of  $1.50 \text{ N/mm}^2$  and successive steps of  $0.65 \text{ N/mm}^2$ . The initial load step corresponds, approximately, to 25% of the compressive strength  $f_c$  obtained from the standard compression tests described in Section 3.3.2, while further load steps correspond, approximately, to 10% of  $f_c$ . The duration of each period under constant load was of three months.

The other four specimens were initially loaded at  $4.10 \text{ N/mm}^2$  (approximately 60% of  $f_c$ ) with subsequent load increases of  $0.65 \text{ N/mm}^2$  (about 10% of  $f_c$ ), applied at intervals of six months. Both load histories adopted have been defined in order that the estimated duration of the tests would be of about two years.

#### *Test results*

Figure 3.13a illustrates the average vertical (longitudinal) and horizontal (transversal) strains obtained for prisms tested with constant load periods of three months. Table 3.10 gives a summary of the experimental results obtained.

For specimens tested with constant load periods of six months, Fig. 3.13b shows the average strain–time diagrams obtained for all tested prisms. In addition, Table 3.11 gives a summary of the results. Figure 3.14 illustrates, as an example, the strain evolution at each face of specimen PRe\_12 and, also, the time–stress–strain diagram for the same specimen. From Fig. 3.14a it is possible to observe that the strain evolution is different at each face of the prism. This behaviour is typical of compression tests in quasi-brittle materials but, in the present experiments, such

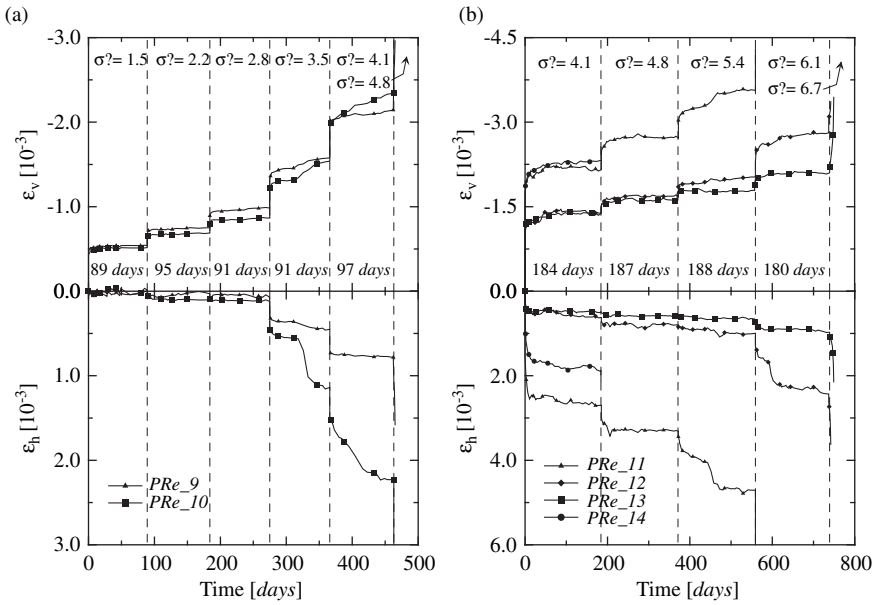


Figure 3.13: Strain–time diagrams obtained from long-term creep tests: (a) constant load periods of three months and (b) constant load periods of six months.  $\sigma$  stands for applied stress in  $N/mm^2$ .

Table 3.10: Results obtained from long-term creep tests with constant load periods of three months.

Specimen	$E$ ( $N/mm^2$ )	$f'_c$ ( $N/mm^2$ )	$T$ (days)
PRe_9	5055	4.75	465
PRe_10	4380	4.75	464
Average	4718	4.8	464

feature is more salient due to the hinged upper loading plate. Another important aspect is that in some specimens cracks suddenly arise during constant load steps, resulting in a strain jump in the strain–time diagram, see, for example, the diagrams of specimen PRe\_10 at 325 days or PRe\_11 at 450 days shown in Fig. 3.13a and b, respectively.

The values obtained for the compressive strength are within the range obtained for the standard compressive strength and short-term creep tests. Displacements recorded with the transducers employed (one per specimen) were found to be in agreement with the strain-gauge measurements.

Figure 3.15 depicts the crack pattern evolution for specimen PRe\_13 as an example. Again, diffuse vertical cracks developing during testing have been



Table 3.11: Results obtained from long-term creep tests with constant load periods of six months (in brackets, the coefficient of variation is given).

Specimen	$E$ (N/mm <sup>2</sup> )	$f'_c$ (N/mm <sup>2</sup> )	$T$ (days)
Pre_11	3720	6.05	559
Pre_12	5055	6.70	742
Pre_13	4345	6.70	749
Pre_14	3270	4.75	184
Average	4100 (19%)	6.0 (15%)	558

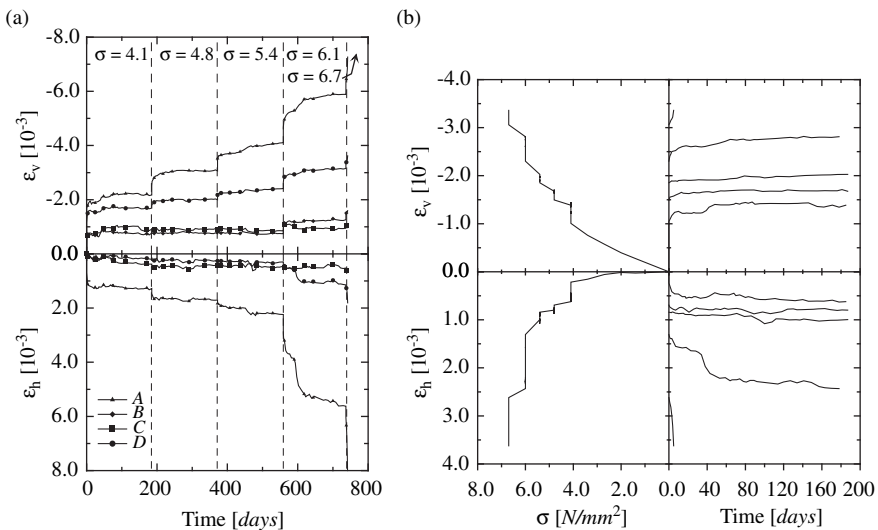


Figure 3.14: Results from long-term creep tests on specimen PRe\_12 (constant load periods of six months): (a) strain evolution for each face and (b) time–stress–strain diagram.  $\sigma$  stands for applied stress in N/mm<sup>2</sup>.

observed, with large cracks and spalling occurring near failure. It is noted that the specimens with lower values of  $f'_c$  presented the most diffused crack patterns. Severe non-uniform distribution of damage can be observed along the four faces of the specimens, confirming the results shown in Fig. 3.14a.

### 3.3.5 Discussion of the results

The short-term compressive strength  $f_c$  of each prism tested in creep is, of course, unknown and can only be estimated. In this section, the peak stress values  $f'_c$



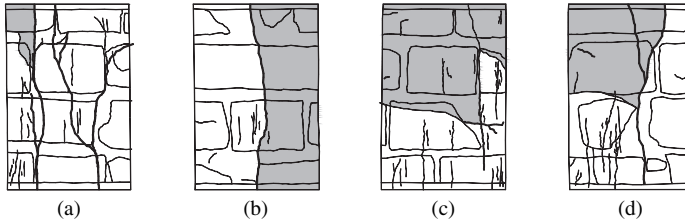


Figure 3.15: Failure pattern for specimen PRe\_13. Shaded areas indicate spalling/loss of material.

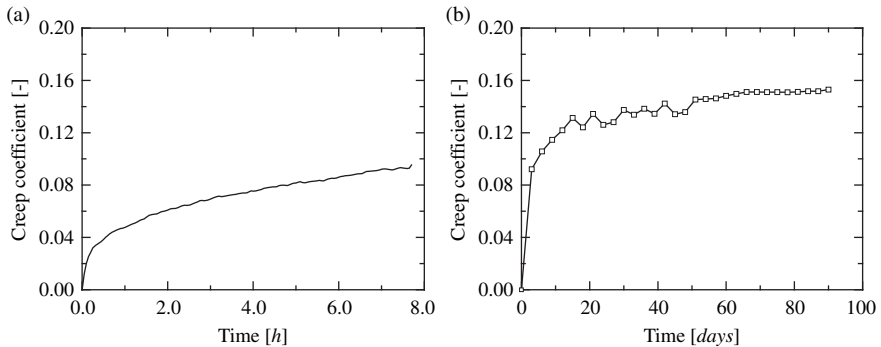


Figure 3.16: Variation of the creep coefficient with time obtained from: (a) short-term creep results and (b) long-term creep results (constant load periods of three months).

obtained from the creep tests are considered as a close estimate of the compressive strength  $f_c$ . Even if, in reality, the compressive strength  $f_c$  does not correspond to  $f'_c$ , such values remain the closest estimate in a material as heterogeneous as the one addressed in this study.

Figure 3.16 illustrates the evolution of the creep coefficient, defined as the ratio between the creep strain and the elastic strain, calculated from the short-term and long-term creep tests results. For each specimen, the creep coefficient was calculated considering all creep diagrams at low stress levels (below 45% of  $f'_c$ ). It is further noted that the creep coefficient obtained from short-term creep tests was calculated from the average of the four tested specimens while the values obtained from long-term creep tests result from the average of the two specimens tested with constant load periods of three months. In the remaining four specimens tested in long-term creep, a first load step of approximately 60% of  $f_c$  was applied and, thus, such tests cannot be used to calculate creep coefficients.

Creep coefficients of approximately 0.10 and 0.15 were found at the end of 8 hours and 90 days of sustained loading, respectively, confirming that most creep

strain occurs at an early stage. Another important aspect is that the creep coefficient found at the end of 90 days is significantly lower than the values recommended by EC6 [28] for masonry made with clay units, which range from 0.5 to 1.0. This can be explained by the fact that EC6 values refer to new masonry, where maturation of mortar is in an initial stage and, also, because the specimens tested had already been under service loads for approximately five centuries prior to testing.

Figure 3.17 shows the strain rate evolution, vertical  $\dot{\epsilon}_v$  and horizontal  $\dot{\epsilon}_h$ , versus the applied stress over strength ratio  $\sigma/f_c'$  for specimens tested in short-term creep. Strain-rate values were calculated between the sixth and eighth hour of each constant load step. It is expected that vertical strain rate values would be negative and horizontal strain rate values positive but some exceptions were found. This can be explained by minor variations in the applied load or changes in the environmental conditions. Such values have been considered equal to zero in the strain-rate diagrams shown in the rest of this section.

In Fig. 3.17a three phases can be distinguished: for low stress levels (up to 50% of  $f_c'$ ), the vertical strain rate is approximately constant and rather low; for medium stress levels (between 50 and 80% of  $f_c'$ ), the vertical strain rate increases at a moderate pace; and, for high stress levels (over 80% of  $f_c'$ ), a remarkable growth of the strain rate stress can be observed. The existence of three distinct phases had also been reported by Mazzotti and Savoia [29] on short-term creep tests performed on concrete specimens. Figure 3.17b shows that beyond 50% of  $f_c'$ , crack growth initiates, influencing the creep behaviour of the material.

Figures 3.18 and 3.19 illustrate the strain rate evolution versus stress over strength ratio for long-term creep tests with constant load periods of three and six months, respectively. Strain rates were calculated from the average results over the last 30 days in the case of the tests with constant load periods of three months and over the last 90 days in the case of tests with constant load periods of six months.

It is noted that the number of results is scarce and further testing is needed to better fundament the observations made. Nevertheless, the difference between the strain rate values obtained from short-term creep tests and long-term creep tests

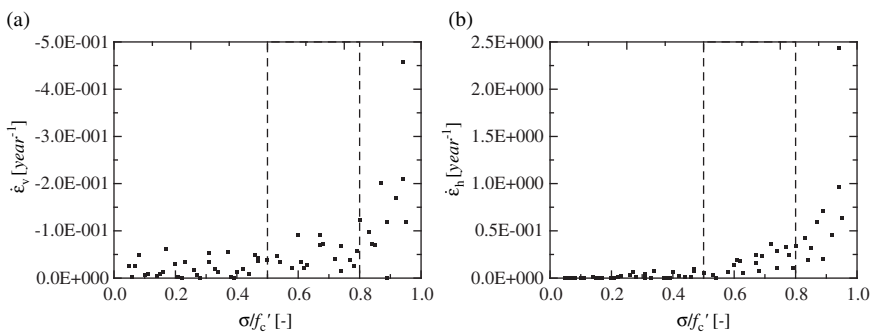


Figure 3.17: Strain rate evolution versus applied stress over strength ratio for short-term creep tests: (a) vertical strain rate and (b) horizontal strain rate.

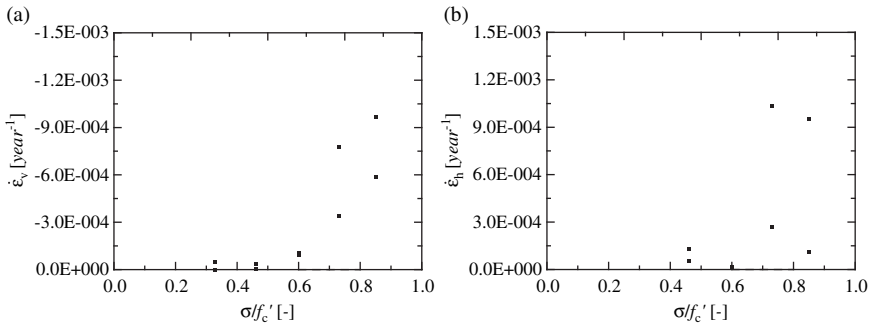


Figure 3.18: Average strain rate over the last 30 days versus applied stress over strength ratio for long-term creep tests (three months steps): (a) vertical strain rate and (b) horizontal strain rate.

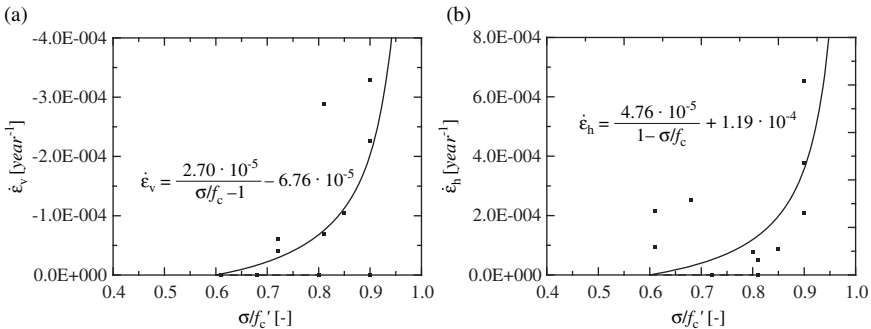


Figure 3.19: Average strain rate over the last 90 days versus applied stress over strength ratio for long-term creep tests (six months steps): (a) vertical strain rate and (b) horizontal strain rate.

is striking. In fact, strain rates ranging from zero to  $-5.0 \times 10^{-1} \text{ year}^{-1}$  were observed in short-term creep tests while in long-term creep tests, values ranging from zero to  $-1.0 \times 10^{-3} \text{ year}^{-1}$  were found. The results obtained from the two types of test seem therefore not comparable. Furthermore, primary creep seems not extinguished at the end of 8 h under sustained loading and, thus, secondary creep rates measured from short-term creep tests must be interpreted carefully.

Another important aspect is that secondary creep was observed to initiate between 60 and 70% of  $f_c'$ . It is further noted that larger strain rate values were obtained for the prisms tested with constant load periods of three months, stressing the scattered nature of the masonry tested.

A hyperbolic least squares fit of the experimental data obtained from the long-term creep tests with constant load periods of six months was computed, which

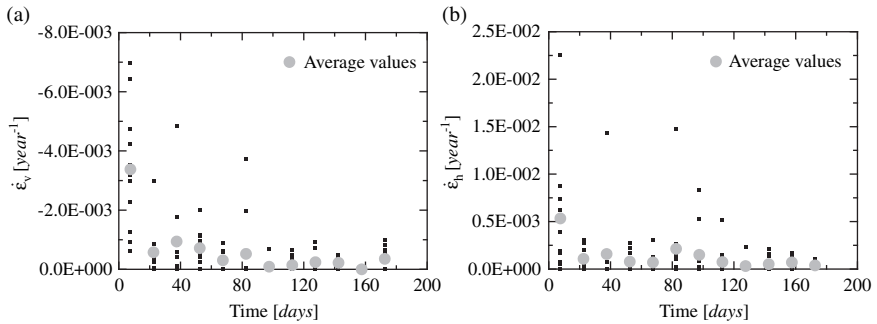


Figure 3.20: Strain-rate evolution in time for applied stresses larger than 60%  $f'_c$ : (a) vertical strain rate and (b) horizontal strain rate.

can be quite useful in calibrating non-linear creep models. The hyperbolic curve adopted is in the following form

$$\dot{\epsilon} = \frac{0.4a}{1 - \sigma/f'_c} + a \quad (1)$$

which yields zero for  $\sigma/f'_c = 0.6$  and has a vertical asymptote for  $\sigma/f'_c = 1.0$ . From the least squares method,  $a = -6.76 \times 10^{-5}$  for the vertical strain rate and  $a = 1.19 \times 10^{-4}$  for the horizontal strain rate.

The striking difference between strain rate values in short-term and long-term creep tests draws attention to what should be the minimum duration of constant load periods when conducting creep tests at high stress levels. A reasonable criterion is believed to be keeping the load constant until only secondary creep is present, i.e. until a fairly constant strain rate is attained. For this purpose, the vertical and horizontal strain rates were calculated for each 15-day period of the total 180 days constant load steps, as illustrated in Fig. 3.20. It is noted that only results corresponding to load levels larger than 60% of  $f'_c$  were considered. The results obtained indicate that the strain rate gets approximately constant after 70–80 days in the case of longitudinal strains and after 30–40 days in the case of transversal strains.

### 3.4 Conclusions and future work

The ability of standard continuum models, based on plasticity and cracking, and of a particle model, consisting in a phenomenological discontinuum approach, to reproduce the experimental compressive behaviour of masonry has been addressed. The comparison between the obtained numerical results and experimental results available in literature allows one to conclude that discontinuum models show clear advantages when compared to standard continuum models in predicting the compressive strength and peak strain of masonry prisms from the properties of



the constituents. Further investigation on models able to provide reliable predictions of masonry compressive strength, accounting for the discrete nature of the masonry components, is therefore suggested.

The creep behaviour under high stresses of ancient regular masonry specimens recovered from the collapsed Civic Tower of Pavia has also been analysed. Standard compression tests, short-term creep tests and long-term creep tests have been conducted. From experimental practice, it is possible to conclude that creep tests on ancient masonry prisms should be carried out by applying the load in successive steps, at a given time interval, starting from a low stress level. In this way, a thorough description of the viscous behaviour of the material can be obtained. Creep tests in which the load is applied in a single step are inadequate in the case of ancient masonry due to the high scatter in the mechanical properties and to the small number of specimens usually available.

The time period between successive load steps should be sufficiently long to extinguish primary creep. In fact, the evolution for different stress levels of the strain rate associated with secondary creep can only be evaluated in such a way. From the results obtained on the regular masonry prisms tested, a minimum time period under sustained loading of 70–80 days should be adopted. For this reason, remarkable differences were observed between secondary creep rates calculated from short-term or long-term creep tests. Short-term creep results should, therefore, be interpreted carefully. Finally, it should be stressed that secondary creep was found to initiate at 60–70% of the compressive strength. A hyperbolic fit to describe the evolution of secondary creep rate with the applied stress-level has been suggested in the present study.

Suggestions for future work include further creep tests so that an adequate characterization of the material can be obtained, given the wide scatter associated with ancient masonry. With respect to the masonry constituents, experimental results on the non-linear creep behaviour of units and mortar are nearly absent in literature [30], meaning that further investigation is required. In terms of numerical modelling, the development of suitable 3D models for viscous inelastic behaviour is needed in order to include time-dependent effects in the numerical simulations of failure.

## References

- [1] Binda, L., Gatti, G., Mangano, G., Poggi, C. & Landriani, G.S., The collapse of the Civic Tower of Pavia: a survey of the materials and structure. *Masonry Int.*, **6**(1), pp. 11–20, 1992.
- [2] Anzani, A., Binda, L. & Mirabella Roberti, G., The effect of heavy persistent actions into the behaviour of ancient masonry. *Materials and Structures*, **33**(228), pp. 251–261, 2000.
- [3] Bazant, Z.P., Material models for structural creep analysis. *Mathematical Modelling of Creep and Shrinkage of Concrete*, ed. Z.P. Bazant, John Wiley & Sons: New York, pp. 99–215, 1988.



- [4] Pickett, G., The effect of change in moisture content on the creep of concrete under a sustained load. *ACI J.*, **38**, pp. 333–355, 1942.
- [5] Neville, A.M., *Properties of Concrete*, John Wiley & Sons: New York, 1997.
- [6] Van Zijl, G.P., *Computational Modelling of Masonry Creep and Shrinkage*. Dissertation, Technical University of Delft, Delft, The Netherlands, 2000.
- [7] Ameny, P., Loov, R.E. & Shrive, N.G., Models for long-term deformation of brick work. *Masonry Int.*, **1**, pp. 27–36, 1984.
- [8] Lenczner, D., Creep and prestress losses in brick masonry. *The Structural Engineer*, **64B(3)**, pp. 57–62, 1986.
- [9] Brooks, J.J., Composite modelling of masonry deformation. *Materials and Structures*, **23**, pp. 241–251, 1990.
- [10] Bazant, Z.P., Current status and advances in the theory of creep and interaction with fracture. *Proc. 5th Int. RILEM Symp. on Creep and Shrinkage of Concrete*, Barcelona, Spain, pp. 291–307, 1993.
- [11] Papa, E., Taliercio, A. & Gobbi, E., Triaxial creep behaviour of plain concrete at high stresses: a survey of theoretical models. *Materials and Structures*, **31**, pp. 487–493, 1998.
- [12] Mazzotti, C. & Savoia, M., Nonlinear creep damage model for concrete under uniaxial compression. *J. Engineering Mechanics*, **129(9)**, pp. 1065–1075, 2003.
- [13] Pina-Henriques, J. & Lourenço, P.B., Masonry compression: a numerical investigation at the meso-level. *Engineering Computations* (accepted for publication).
- [14] Binda, L., Fontana, A. & Frigerio, G., Mechanical behaviour of brick masonries derived from unit and mortar characteristics. *Proc. 8th Int. Brick and Block Masonry Conf.*, Dublin, Ireland, Vol. 1, pp. 205–216, 1988.
- [15] Frigerio, G. & Frigerio, P., *Influence of the Components and Surrounding Environment in the Mechanical Behaviour of Brick Masonry* (in Italian). Graduation thesis, Politecnico di Milano: Milan, Italy, 1985.
- [16] Mann, W. & Betzler, M., Investigations on the effect of different forms of test samples to test the compressive strength of masonry. *Proc. 10th Int. Brick and Block Masonry Conf.*, Calgary, Canada, pp. 1305–1313, 1994.
- [17] Berto, L., Saetta, A., Scotta, R. & Vitaliani, R., Failure mechanism of masonry prism loaded in axial compression: computational aspects. *Materials and Structures*, **38(276)**, pp. 249–256, 2005.
- [18] Pina-Henriques, J. & Lourenço, P.B., Testing and modelling of masonry creep and damage in uniaxial compression. *Proc. 8th Int. Conf. Structural Studies, Repairs and Maintenance of Heritage Architecture*, Halkidiki, Greece, pp. 151–160, 2003.
- [19] Rots, J.G., *Computational Modelling of Concrete Fracture*. PhD Dissertation, Delft University of Technology, Delft, The Netherlands, 1988.
- [20] DIANA Finite Element Code, version 8.1. TNO Building and Construction Research, Delft, The Netherlands.
- [21] Vermeer, P.A. & de Borst, R., Non-associated plasticity for soils, concrete and rock. *Heron*, **29(3)**, pp. 1–64, 1984.



- [22] Lourenço, P.B., *A User/Programmer Guide for the Micro-Modelling of Masonry Structures*. Report 03.21.1.31.35, Delft University of Technology, Delft, The Netherlands, 1996. Available from <http://www.civil.uminho.pt/masonry>.
- [23] CEB-FIP Model Code 1990; Bulletin D'Information No. 213/214, Comité Euro-International du Béton, Telford: London, 1993.
- [24] Lourenço, P.B. & Rots, J.G., A multi-surface interface model for the analysis of masonry structures. *J. Engineering Mechanics*, ASCE, **123**(7), pp. 660–668, 1997.
- [25] Lourenço, P.B., *Computational Strategies for Masonry Structures*. PhD Dissertation, Delft University of Technology, Delft, The Netherlands, 1996. Available from [www.civil.uminho.pt/masonry](http://www.civil.uminho.pt/masonry).
- [26] van der Pluijm, R., *Out-of-plane Bending of Masonry: Behaviour and Strength*. PhD Dissertation, Eindhoven University of Technology, Eindhoven, The Netherlands, 1999.
- [27] Anzani, A., Binda, L. & Melchiorri, G., Time dependent damage of rubble masonry walls. *Proc. British Masonry Society*, **2**(7), pp. 341–351, 1995.
- [28] Eurocode 6: Design of masonry structures; prEN 1996-1-1:2002, CEN: Brussels, Belgium, 2003.
- [29] Mazzotti, C. & Savoia, M., Nonlinear creep, Poisson's ratio, and creep-damage interaction of concrete in compression. *ACI Materials J.*, **99**(5), pp. 450–457, 2002.
- [30] Papa, E., Binda, L. & Nappi, A., Effect of persistent loads in masonry structures. *Proc. 3rd Int. Masonry Conf.*, London, pp. 290–294, 1992.

